

Approaching the ultrastrong coupling regime between an Andreev level and a microwave resonator

O.O. Shvetsov,* A. Khola, V. Buccheri, I.P.C. Cools, N. Trnjanin, and A. Geresdi
*Department of Microtechnology and Nanoscience,
Chalmers University of Technology, SE-41296 Gothenburg, Sweden*

T. Kanne and J. Nygård
*Niels Bohr Institute, Center for Quantum Devices, University of Copenhagen,
Universitetsparken 5, DK-2100 Copenhagen O, Denmark*
(Dated: February 14, 2025)

Josephson junctions formed in semiconductor nanowires host Andreev bound states and serve as a physical platform to realize Andreev qubits tuned by electrostatic gating. With the Andreev bound state being confined to the nanoscale weak link, it couples to a circuit-QED architecture via the state-dependent supercurrent flowing through the weak link. Thus, increasing this coupling strength is a crucial challenge for this architecture. Here, we demonstrate the fabrication and microwave characterization of an InAs nanowire weak link embedded in a superconducting loop with a lumped-element resonator patterned from a thin NbTiN film with high kinetic inductance. We investigated several devices with various weak link lengths and performed spectroscopy of spin-degenerate and spin-orbit split Andreev bound states for the shorter and longer weak links, respectively. Our approach offers a compact geometry and a large resonator impedance above 12 k Ω at a resonator frequency of 8 GHz, which results in a measured coupling strength reaching 1.95 GHz to the Andreev level and 77 MHz to the Andreev spin. Our spectroscopic data are in good agreement with existing theoretical models and demonstrate ultrastrong coupling to the Andreev pair qubit with the coupling strength approaching the bare resonator and qubit frequencies.

I. INTRODUCTION

Circuit-QED (cQED) describes the interaction of photons stored in a superconducting resonator and a two-level system (qubit) [1]. The latter is often based on a single electron spin [2] or collective excitations in various superconducting circuits [3, 4]. For quantum information processing, the favorable regime is when the qubit is strongly coupled to the resonator, that is, when they exchange a photon many times before the coherence is lost [4].

A distinct ultrastrong coupling regime is established when the coupling strength becomes a significant fraction of the bare resonator and qubit frequencies [5]. In this case, the common rotating-wave approximation is no longer valid and more comprehensive perturbative models are applied [6]. The ultrastrong coupling regime is of practical relevance to quantum technologies, where it can be used, e.g., for ultrafast quantum computation [7].

Andreev bound states (ABSs) are discrete fermionic excitations spatially confined in a weak link between two superconductors [8, 9]. Atomic-like transitions between these states can be utilized for the realization of two types of qubits: Andreev pair qubit [10–12] and Andreev spin qubit [13–15], which can be experimentally investigated by the means of cQED techniques [16]. Semiconductor nanowires serve as a preferred platform for such experiments, due to a high material quality, gate tunability and

intrinsically strong spin-orbit coupling [17], which opens up the possibility of exploiting not only the charge, but also the spin degree of freedom in qubit applications. All this makes Andreev qubits a promising compromise between spin and superconducting qubits, combining the advantages of both types in one platform [18–20].

Unlike conventional superconducting circuits, which rely on collective excitations coupled to the electromagnetic environment of the qubit, ABSs are localized in the weak link and carry a supercurrent up to the range of 10 nA for a typical geometry of InAs/Al nanowires [21]. This makes it more challenging to reach a strong coupling to a microwave resonator. In practice, the coupling is typically realized by embedding a phase-biased weak link in a superconducting loop with a part of the resonator, also referred to as a shared inductance. In this case, the coupling rate g_c is proportional to the zero-point flux (phase) fluctuations across the shared inductance [16], which is in turn proportional to the square root of the resonator impedance Z_r , resulting in $g_c \propto \sqrt{Z_r}$ [22, 23]. Thus, an increase in the resonator impedance naturally leads to a stronger coupling, enabling better resolution spectroscopy and making higher energy states accessible.

In this paper, we investigate several devices that integrate a high-impedance lumped-element resonator and an Al/InAs nanowire weak link. Due to the high kinetic inductance of the NbTiN thin film, the differential impedance of the resonator reaches values above 12 k Ω . Microwave spectroscopy of the devices revealed both spin-degenerate and spin-orbit split ABSs. We achieve an ultrastrong coupling between the resonator and a single ABS with a coupling strength up to 1.95 GHz, that

* shvetsov@chalmers.se

is more than 20% of the bare resonator frequency. Moreover, we demonstrated that the presented geometry can be used to couple to an Andreev spin with a coupling strength of 77 MHz. The experimental data are consistent with existing theoretical models.

II. DEVICE AND SETUP

The devices used in this work consist of an Al/InAs nanowire weak link [17] embedded in a superconducting loop with a high-impedance lumped-element resonator. We report on fabrication and measurement of 3 devices, where the resonator geometry and the weak link length vary. Their parameters are listed in Table I. A representative Device 2 is demonstrated in Fig. 1(a) and described below.

The resonator is patterned on a sapphire substrate with a thin (around 4 nm) film of highly disordered NbTiN superconductor. The resonator consists of a differential pair of 130 nm wide and $38.3 \mu\text{m}$ long symmetric arms, divided by the grounding strip in the middle. Each arm is terminated with a triangular-shaped capacitor plate that is coupled to a 50Ω feedline. Due to the high kinetic inductance of the thin film $L_{k,\square} \approx 400 \text{ pH}$, this compact structure with a footprint of $50 \times 50 \mu\text{m}^2$ realizes a total inductance $L_r \approx 118 \text{ nH}$ and resonates at the frequency $f_r = 8.619 \text{ GHz}$ as a non-distributed lumped-element resonator. The differential impedance of the resonator reaches $Z_{r,diff} = 2\sqrt{\frac{L_r}{C_r}} \approx 12.76 \text{ k}\Omega$.

The weak link was defined in a 150 nm thick MBE-grown InAs nanowire with an in-situ grown epitaxial Al shell covering three of its facets [17]. A 250-450 nm long part of the 27 nm thick Al shell was removed by wet etching [24], an example is shown in the Inset to Fig. 1(a). A small part of the resonator with the shared inductance $2l \approx 12.3 \text{ nH}$ is coupled to the nanowire by incorporating it in a common superconducting loop with Al contacts. In this geometry, the coupling between the ABSs and the resonator is proportional to the zero-point flux fluctuations across the shared inductance $\Phi_{zpf} = \frac{l}{L_r} \sqrt{\frac{\hbar Z_{r,diff}}{2}} \approx 0.021 \Phi_0$, where $\Phi_0 = h/2e$ is the superconducting flux quantum. The shared inductance was intentionally designed to be large, but comparable to the weak link Josephson inductance, which ensures that the phase across the junction φ is a nonhysteretic function of the applied flux Φ . Moreover, our analysis shows that $\varphi \approx 2\pi\Phi/\Phi_0$ is a reasonable approximation (see Appendix D).

A DC electrostatic side gate is defined at the distance of 150 nm apart from the junction to tune the electrochemical potential in the nanowire. The differential drive and the overall symmetric chip layout ensure that along the mirror line, the AC electric field is essentially zero. To reference the nanowire to the DC ground potential, the nanowire loop is connected to the ground by a metal strip located along this line, which does not disturb the res-

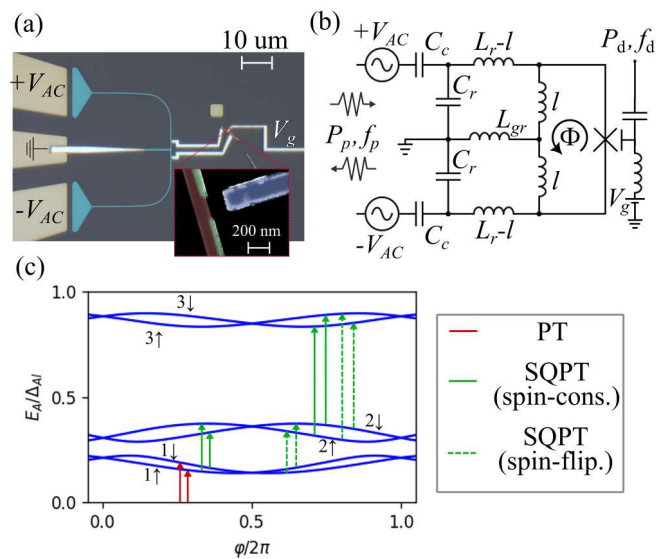


FIG. 1. (a) An optical micrograph of Device 2. The resonator is represented by a blue (false-color) U-shape structure patterned from a thin NbTiN film with high kinetic inductance. The resonator is capacitively coupled to a pair of feedlines. An Al/InAs nanowire weak link is defined close to the mirror line of the device and coupled to the resonator by aluminum contacts. The inset demonstrates a false-color electron micrograph of the nanowire weak link with the side gate. (b) Circuit diagram shows an equivalent lumped-element scheme of the device. It consists of a differential pair of resonators with the inductances L_r and capacitances C_r , coupled to the feedlines by the capacitors C_c . The nanowire weak link is embedded in a flux-biased superconducting loop with a small fraction of the resonator with the shared inductance $2l$. To ground the loop, the resonator's middle part is connected with the ground plane. The resonator is probed in reflection with the probe signal of power P_p and frequency f_p . The side gate is used to tune the nanowire's electrochemical potential and to excite the system with a drive signal of power P_d and frequency f_d . (c) Typical excitation spectrum of a long weak link with spin-orbit interaction. Three ABSs are present in the spectrum, each of them is split into a doublet of states with the opposite pseudo-spin, denoted by \uparrow and \downarrow . Microwave photons can induce pair transitions (PT, red arrows) and single-quasiparticle transitions (SQPT, green arrows), where for the latter spin-conserving (solid) and spin-flipping (dashed) processes can be distinguished. The energy scale is normalized to the superconducting gap in Al.

onator's odd mode. In such a design, having the nanowire weak link defined at the zero AC voltage line is preferable to mitigate microwave losses through the side gate. A superconducting coil was used to flux bias the weak link. The circuit diagram of the device is presented in Fig. 1(b).

The odd mode of the resonator is probed in reflection with the signal of power P_p and frequency f_p . A separate microwave tone passes through a bias tee to the side gate to excite the system with a drive signal of power P_d and frequency f_d .

TABLE I. Parameters of the devices, including length, width and differential impedance of the resonators, thin film kinetic inductance, bare resonator frequency, zero-point flux fluctuations across the shared inductance and the weak link length.

Device	Length, μm^{a}	Width, nm	$Z_{r,diff}$, $\text{k}\Omega$	$L_{k,\square}$, pH^{b}	f_r , GHz	Φ_{zpf} , Φ_0^{c}	l_{wl} , nm
1	48.3	130	12.28	320	8.2230	0.016	250
2	38.3	130	12.76	400	8.6190	0.021	320
3	53.3	130	13.27	345	7.4685	0.015	450

^a Length of one arm of the differential pair.

^b May vary due to the sample ageing and slightly different fabrication parameters.

^c Deduced from the resonator geometry and inductance.

After fabrication, the device chip is wire bonded to a printed circuit board and embedded in a copper box attached to the mixing chamber of a dilution refrigerator with a base temperature of 10 mK. To screen spurious magnetic fields in the laboratory, an additional aluminum shield wrapped with magnetic shielding foil was installed.

The system represents a typical cQED setup, where microwave photons drive transitions between ABSs, and the state of the system can be detected by the resonator dispersive shift. One of the defining parameters of the ABS spectrum in a weak link is the ratio between the weak link length l_{wl} and the superconducting coherence length ξ , which is typically several hundred nanometers in Al/InAs nanowires. To describe the excitation spectrum in a finite-length weak link with $l_{wl}/\xi \sim 1$, we refer to the model employed in Ref. [14, 25]. The minimal model that includes spin-orbit splitting requires two transverse subbands, in this case the ABSs' energy dispersion $\epsilon = E_A/\Delta_{Al}$ is a solution to the transcendental equation:

$$\begin{aligned} \tau \cos[(\Lambda_1 - \Lambda_2)\epsilon \mp \varphi] + (1 - \tau) \cos[(\Lambda_1 + \Lambda_2)\epsilon x_0] &= \\ = \cos[2 \arccos \epsilon - (\Lambda_1 + \Lambda_2)\epsilon], \end{aligned} \quad (1)$$

where τ is the channel transmission, Δ_{Al} is the Al superconducting gap, $x_0 \in [-1, 1]$ indicates the position of a barrier in the weak link (normalized to $l_{wl}/2$), and $\Lambda_j = l_{wl}\Delta_{Al}/\hbar v_{Fj}$, where v_{Fj} is the Fermi velocity of the subband $j = 1, 2$ in the nanowire.

In a finite-length weak link, multiple ABSs can squeeze into the spectrum, e.g., three levels are shown in a characteristic spectrum illustrated in Fig. 1(c). Spin-orbit interaction lifts the spin degeneracy, splitting each of the states into a doublet with the opposite pseudo-spin, denoted by \uparrow and \downarrow . The time-reversal symmetry preserves degeneracy only at $\varphi = 0$ and $\varphi = \pi$. We consider two types of transitions: a pair transition (PT, red arrows) takes place when two quasiparticles are excited from the ground state; a single-quasiparticle transition (SQPT, green arrows) occurs when a quasiparticle that is already present in the system is promoted to one of the upper levels. Among SQPTs, spin-conserving (solid) and spin-flipping (dashed) transitions can be distinguished, when the transition is between the levels with the same or opposite pseudo-spin, respectively.

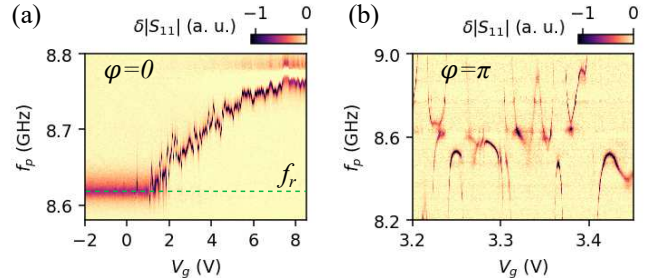


FIG. 2. Change in the absolute value of the resonator reflection $\delta|S_{11}|$ as a function of the probe frequency f_p and gate voltage V_g measured in Device 2 at $\varphi = 0$ in (a) and at $\varphi = \pi$ in (b). The line at $f_r = 8.619$ GHz in (a) denotes the bare resonator frequency, when the nanowire is fully pinched off. The gate-independent background was subtracted.

III. RESULTS AND DISCUSSION

We first present the typical microwave gate response, obtained for Device 2. The change in the absolute value of the resonator reflection $\delta|S_{11}|$ as a function of the probe frequency f_p and side-gate voltage V_g is presented in Fig. 2 (the gate-independent background is subtracted). In (a), the phase across the weak link φ is fixed at zero, while $\varphi = \pi$ in (b). The junction is fully pinched off below $V_g \approx 1$ V, where the resonance approaches the bare resonator frequency $f_r = 8.619$ GHz. The data obtained at $\varphi = \pi$ in (b) demonstrates multiple avoided crossings, signifying that highly transmissive ABSs are strongly coupled to the resonator mode.

Further, we performed single- and two-tone spectroscopy to characterize the system. To mitigate charge noise and avoid electrostatic drifting, in these measurements we fix the gate voltage V_g at one of the points where the resonator gate response has a local extremum, such as one of those observed in Fig. 2(b). Single-tone spectra are taken by sweeping the probe frequency f_p of power P_p and measuring S_{11} complex parameters at various applied fluxes. The flux-independent background was subtracted in the data plotted. In two-tone spectroscopy, the continuous probe signal is fixed at resonance, and S_{11} is measured as a function of phase (flux) and drive tone with frequency f_d and power P_d . To reference the signal measured in two-tone spectra, we subtracted a drive

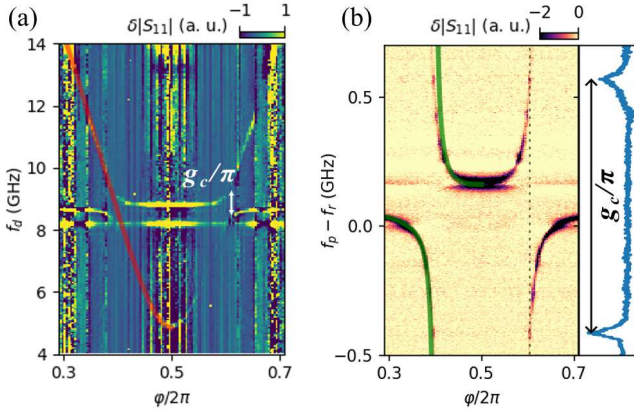


FIG. 3. (a) Two-tone spectrum measured in Device 2 at $V_g = 3.39$ V. The fit of the PT frequency as a function of phase is shown by the red line. The spectrum reveals avoided crossings at $\varphi/2\pi = 0.4$ and $\varphi/2\pi = 0.6$ with the coupling at the crossing point $g_c/2\pi \approx 490$ MHz, denoted by the white arrow. A flat line seen at around 8.1 GHz corresponds to the resonator's even mode, which is insensitive to the state of the weak link. (b) Corresponding single-tone spectrum. The probe frequency f_p is offset to the bare resonator frequency $f_r = 8.619$ GHz. The green line represents the fit of the resonator shift. The cross-section on the right side clearly confirms $g_c/2\pi \approx 490$ MHz at the avoided crossing (along the gray dotted line in (b)).

frequency-independent background.

A. Spectroscopy of spin-degenerate ABSs

Fig. 3 presents the spectroscopy data for Device 2. Data were acquired at $V_g = 3.39$ V and at the nominal powers $P_p \approx -130$ dBm and $P_d \approx -100$ dBm. The left panel illustrates the two-tone spectrum, which reveals a PT arising from a highly transmissive spin-degenerate ABS. It crosses the odd mode of the resonator, forming a pair of avoided crossings at $\varphi/2\pi = 0.4$ and $\varphi/2\pi = 0.6$, where the coupling can be directly extracted from the distance between the levels $g_c/2\pi \approx 490$ MHz.

In the vicinity of $\varphi = \pi$, the PT frequency can be fitted to the dispersion relation valid for a short weak link:

$$hf_{PT} = 2E_A = 2\Delta' \sqrt{1 - \tau \sin^2(\varphi/2)} \quad (2)$$

in respect that the effective gap value in a finite-length weak link is smaller than the gap in aluminum $\Delta' < \Delta_{Al}$ (see Appendix C for details). The least-squares method yields $\Delta'/h = 11.688 \pm 0.026$ GHz and $\tau = 0.95694 \pm 0.00045$. The resulting fit is represented as a red line in Fig. 3(a).

Fig. 3(b) shows the corresponding single-tone spectrum. The coupling at the avoided crossing $g_c/2\pi \approx 490$ MHz can be directly extracted from the line-cut along the gray dotted line, see the cross-section on the

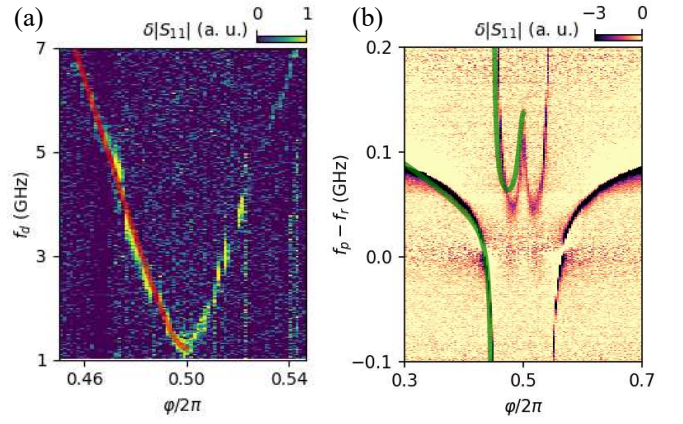


FIG. 4. (a) Two-tone spectrum measured in Device 1 at $V_g = 14.5$ V. The PT frequency fit plotted as a function of phase is denoted by the red line. (b) Corresponding single-tone spectrum. The probe frequency f_p is offset to the bare resonator frequency $f_r = 8.223$ GHz. The green line denotes the fit of the resonator shift.

right side of the plot. The green line denotes the fit that was obtained from the model described in Appendix C. The fit relies on a single ABS observed in the two-tone spectrum in Fig. 3(a), and we used the zero-point flux fluctuations across the shared inductance as the only fitting parameter. The least-squares fit to the experimental data yields $\Phi_{zpf} = (0.02816 \pm 0.00018)\Phi_0$, which slightly overshoots the value obtained from the geometry analysis, see Table I. To validate the fit, we extract from it the magnitude of the coupling at the avoided crossing point $g_c/2\pi = 495.3 \pm 3.8$ MHz, which is in good agreement with the experimental data. The maximum coupling can be extracted at $\varphi = \pi$: $g_c/2\pi = 967.5 \pm 6.7$ MHz.

Fig. 4 provides the spectroscopy data, obtained for Device 1 with the shortest 250 nm weak link at $P_p \approx -130$ dBm and $P_d \approx 100$ dBm, and at $V_g = 14.5$ V (this device required larger gate voltage due to the longer distance to the gate). Here, we were following a similar fitting routine. The two-tone spectrum in Fig. 4(a) is fitted by Eq. (2) describing a PT arising from a single high-transmission channel. The best fit reveals $\tau = 0.999416 \pm 0.000062$ and $\Delta'/h = 25.24 \pm 0.23$ GHz. The manifestation of an ABS with a very large transmission in single-tone spectroscopy in Fig. 4(b) is a sharp peak at $\varphi = \pi$ [16]. This feature is well described within the presented model with $\Phi_{zpf} = (0.02466 \pm 0.00024)\Phi_0$ as the only fitting parameter, and we extract the maximum coupling $g_c/2\pi = 1.953 \pm 0.018$ GHz at $\varphi = \pi$.

B. Spectroscopy of spin-resolved ABSs

SQPTs associated with spin-split ABSs were routinely observed for Devices 2 and 3 with longer weak links.

Fig. 5(a-d) provides the spectroscopy data obtained for Device 3 at $V_g = 1.498$ V and for Device 2 at $V_g = 2.44$ V

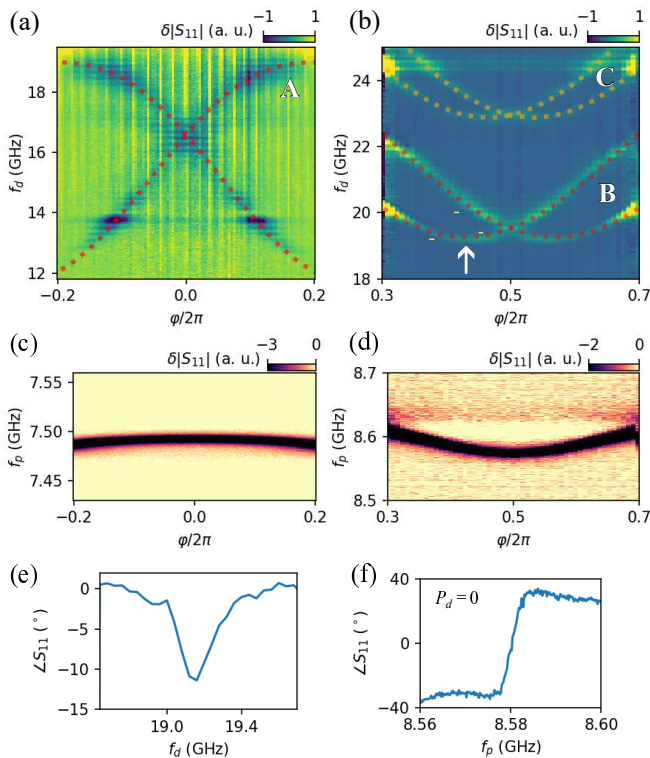


FIG. 5. Spectroscopy data obtained for Device 3 at $V_g = 1.498$ V (a, c) and for Device 2 at $V_g = 2.44$ V (b, d). In two-tone spectra (a, b), bundles of SQPTs are observed, with crossings at the degeneracy points. SQPT frequency fits are denoted by the dotted lines and labeled as A, B and C. The fit parameters are listed in Table II. d) Corresponding single-tone spectra indicating the dominance of the even parity ground state. (e) Phase of the reflected signal as a function of the drive frequency at a minimum of the lower SQPT, see the white arrow in (b). (f) Corresponding resonator response when the system is not excited.

around the degeneracy points $\varphi = 0$ and $\varphi = \pi$, respectively. Panels (a) and (b) illustrate two-tone spectroscopy data that reveal bundles of 4 lines, which we assign to spin-conserving SQPTs, see Fig.1(c).

The corresponding single-tone spectra in Fig. 5(c, d) clearly indicate the even parity ground state of the system [11, 16, 26], signifying that our devices are weakly poisoned by non-equilibrium quasiparticles. An SQPT requires that a quasiparticle is trapped at one of the ABSs [14, 27]. Previous reports have revealed that parity switching events occur on a timescale of ~ 0.1 ms [11, 27], which is much shorter than a ~ 1 s integration time used in the measurements. This means that during the measurement, the weak link is free of non-equilibrium quasiparticles most of the time, which significantly reduces the SQPT line contrast and hinders the observation of spin-split ABSs. Nevertheless, in the ultrastrong coupling regime, it was feasible to resolve these states, despite the fact that the system is weakly poisoned, and the readout frequency was always fixed at the even par-

ity ground state resonance, as it was the only one clearly visible in the single-tone spectra.

The spectroscopic lines in Fig. 5(a) can be fitted with the transitions between the two lowest Andreev doublets ($1\uparrow \Rightarrow 2\uparrow$ and $1\downarrow \Rightarrow 2\downarrow$). Parameters which provide the best fit were obtained by the least-squares method applied to transitions between the ABSs given by Eq. (1), see Appendix C for details. These parameters are listed in Table II, column A. The fit is shown by the red dotted line.

In Fig. 5(b), two bundles of lines are observed. Each of those take place at relatively large frequencies above 19 GHz and have an upward curved shape, which implies that the transitions occur between the upper doublets ($2\uparrow \Rightarrow 3\uparrow$ and $2\downarrow \Rightarrow 3\downarrow$). The parameters provided by the least-squares method are listed in Table II, where B corresponds to the red dotted line, and C to the orange one in Fig. 5(b), respectively.

The coupling between the resonator and a spinful ABS can be estimated from the line shape of a SQPT. Fig. 5(e) shows the phase of the reflected signal as a function of the drive frequency at a minimum of the lower SQPT in Fig. 5(b) (marked by an arrow). The phase shift induced by this transition is $\delta(\angle S_{11}) \approx 10^\circ$. Basing on the corresponding resonance line shape of a non-excited system (Fig. 5(f)), the phase shift can be converted to the resonator frequency shift $\delta f_r^{SQPT} \approx 770$ kHz. This is a considerably larger shift compared to a typical value of tens of Hz reported previously [14]. The shift can be described by second-order perturbation theory [15]:

$$\delta f_r^{SQPT} \approx \left(\frac{g_c}{2\pi}\right)^2 \frac{2f_{SQPT}}{f_{SQPT}^2 - f_r^2},$$

from which we extract the spin-photon coupling $g_c/2\pi \approx 77$ MHz. This value is comparable to the recently reported strong coupling between a high-impedance resonator and a singlet-triplet spin qubit [28]. We should note that the measured dispersive shift δf_r^{SQPT} is the average over a long time compared to the parity switching rate, thereby the actual coupling to an Andreev spin is likely to be larger.

In our experiment, we repeatedly observed that only spin-conserving SQPTs are clearly visible in the spectra. This is in agreement with the general selection rules: in the presence of transverse symmetry in the nanowire, spin-flipping transitions should be suppressed. However, previous studies showed that spin-flipping transitions can

TABLE II. A table of parameters for the SQPT fits in Fig. 5(a, b). Δ_{AI}/h is fixed at 52 GHz.

	A	B	C
Λ_1	5.74 ± 0.31	2.439 ± 0.071	2.84 ± 0.13
Λ_2	1.52 ± 0.31	3.064 ± 0.089	3.16 ± 0.13
τ	0.347 ± 0.043	0.2432 ± 0.0088	0.2645 ± 0.0058
x_0	0.4894 ± 0.0054	0.26154 ± 0.00011	-0.000837

still be excited at elevated drive powers in a realistic non-ideal device [14, 15]. For example, the gate drive can violate transverse symmetry and unlock spin-flipping transitions [16, 29, 30]. Although we used the gate drive in our setup, we did not observe spin-flipping SQPTs. This is most likely because we had to operate at sufficiently low drive powers, so that the thin film resonator is not driven into a non-linear regime.

IV. CONCLUSION

In conclusion, we demonstrated a robust approach for achieving a large coupling strength between a high-impedance lumped element resonator and ABSs residing in an Al/InAs nanowire weak link. We performed spectroscopy of multiple devices with various weak link lengths, showing that spin-degenerate and spin-orbit split ABSs are strongly coupled to the resonator mode. Our results are supported by a good agreement with the existing theoretical models. The presented approach can be further extended to facilitate a strong qubit-qubit coupling in a device comprising multiple Andreev qubits and to increase the coupling to the Andreev spin transitions.

V. ACKNOWLEDGMENTS

This work was financially supported by the European Union's H2020 research and innovation program, grants №804988 (SiMS) and №828948 (AndQC) and by the Army Research Office (ARO) grant W911NF2210053. The Center for Quantum Devices is supported by the Danish National Research Foundation grant №DNRF101, the Novo Nordisk Foundation project SolidQ and the Carlsberg Foundation. The devices were fabricated in the Myfab cleanroom at Chalmers, and technical support from Nanofabrication Laboratory is gratefully acknowledged. We also thank P. Makk, S. Csonka, G. Fülöp and V. Fatemi for fruitful discussions.

Appendix A: NbTiN thin film high kinetic inductance and the resonator impedance

DC transport characterization of a test resonator structure (a replica of Device 1) provides NbTiN thin film normal state sheet resistance $R_{N,\square} = 1.46 \text{ k}\Omega$ and critical temperature $T_c = 6 \text{ K}$. With these parameters, we can estimate the sheet kinetic inductance as $L_{k,\square}^{DC} \approx \frac{\hbar R_{N,\square}}{\pi \Delta}$ [31], where $\Delta \approx 1.76 k_B T_c$ is the superconducting gap linked to T_c by a standard BCS prediction [32]. This yields $L_{k,\square}^{DC} \approx 320 \text{ pH}$.

In addition, for each of the devices, we performed microwave domain simulations for the actual geometries used in the experiment. To simulate a bare resonator, we replaced the weak links with a short break in the film, but

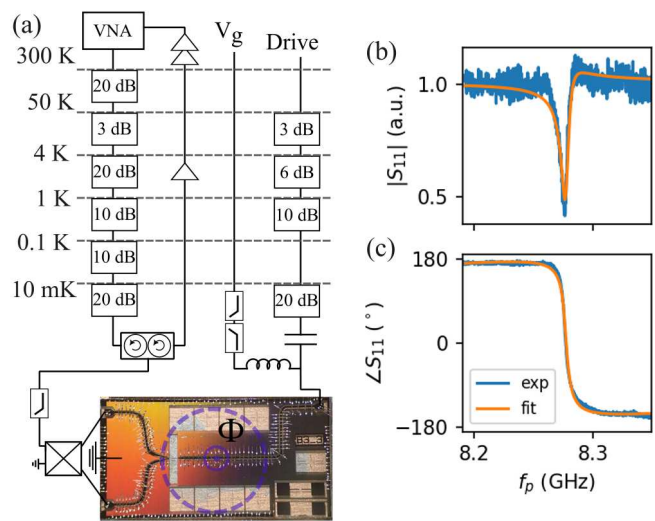


FIG. 6. (a) Experimental setup. (b, c) Reflected signal amplitude (phase) versus probe tone frequency for one of the devices at zero external flux (the ABSs are far detuned). The blue line shows the experimental data. The orange line represents the fit, revealing $Q_i \approx 3800$ and $Q_c \approx 1000$.

all the aluminum structures were included because they contribute to the total stray capacitance of the resonator. We extracted $L_{k,\square}$ from the best fits of the simulated resonator microwave response to the experimental data at low V_g , when the nanowires are fully depleted. The results are listed in Table I, see the main text. Since all resonators were picked up from the same batch with the same NbTiN thickness, we attribute the variation in $L_{k,\square}$ to the aging of the sample and slightly different fabrication parameters used during nanowire processing (e.g., it was observed that the resulting $L_{k,\square}$ depends on the baking temperature of the resist).

The total inductance L_r (for one arm of the differential pair) is derived from the geometry and $L_{k,\square}$ is obtained as described above. The bare resonator frequency f_r is obtained experimentally. The differential impedance is defined as $Z_{r,diff} = 2\sqrt{\frac{L_r}{C_r}} = 4\pi f_r L_r$.

We note that we routinely observed the resonator's even mode, which is insensitive to the weak link's state and positioned at several hundred MHz below the odd mode, yielding a flat line at around 8.1 GHz in Fig. 3. We confirmed the even mode frequency by microwave domain simulations. Its frequency is determined by $2\pi f_r^{even} = 1/\sqrt{(L_r + 2L_{gr})C_r}$, where $L_{gr} \approx 10 \text{ nH}$ is the inductance of the grounding strip, which connects the ground plane and the middle part of the resonator, see Fig. 1(a, b).

Appendix B: Measurement setup

The measurement scheme is depicted in Fig. 6(a). The microwave readout tone passes through an attenuated

line and a double circulator located at the mixing chamber stage, and then routed through a 180° hybrid to differentially drive two on-chip 50Ω feedlines capacitively coupled to the resonator. The readout tone is reflected off the resonator's odd mode and routed through a series of cryogenic and room temperature amplifiers. The complex reflection parameter (S_{11}) is measured by a vector network analyzer. A separate microwave tone pass through the gate line to drive the ABS transitions, where a bias tee is used to combine the DC gate voltage and the drive tone. Fig. 6(b, c) represents the characteristic S_{11} response of one of the devices when the ABSs are far detuned (at zero applied flux). The resonance is fitted by the diameter-correction method [33], which yields the internal quality factor $Q_i \approx 3800$ and the coupling quality factor $Q_c \approx 1000$ when the ABSs are far detuned. We would like to emphasize that in our setup, the large coupling magnitude results in a significant magnetic flux dependence of the internal quality factor when the Andreev level energy approaches the bare resonator frequency. At $\varphi = \pi$ the nanowire introduces maximum losses to the system, and Q_i usually drops to around 1000.

Appendix C: Details of the fitting routine

1. Fitting of SQPTs

SQPT frequency can be found from Eq. (1) (see the main text) as a difference between the energies of the two neighboring states. In our fitting routine, we first performed manual parameter selection to obtain a reasonable fit. Then, these parameters were used as an initial guess to the least-squares method. We found that the set of parameters is not always unique, which can produce large uncertainties. Furthermore, we frequently observed significant correlations between parameters, such as the correlation between x_0 and Δ_{Al} , which could reach almost 100%. This is likely because both parameters are responsible for the overall energy scale. In order to mitigate these concerns, we fixed the gap parameter $\Delta_{Al}/h = 52$ GHz for all the fits depicted in Fig. 5. This appeared to be a satisfactory initial parameter guess for each fit.

2. Spin-degenerate states

The dispersion relation in Eq. (1) can be simplified to describe PTs in a finite-length weak link. For a PT, we detect the average of a spin-split Andreev doublet and we can neglect spin-orbit coupling assuming that $\Lambda_1 = \Lambda_2 = \Lambda$. Expansion of Eq. (1) around $\varphi = \pi$ up to second order in ϵ recovers the short-junction expression:

$$E_A(\varphi) \approx \Delta' \sqrt{1 - \tau \sin^2(\varphi/2)}, \quad (\text{C1})$$

with

$$\Delta' = \frac{\Delta_{Al}}{\sqrt{(1 + \Lambda)^2 + (x_0 \Lambda \sqrt{1 - \tau})^2}}. \quad (\text{C2})$$

To fit the resonator frequency shift in single-tone spectra, we use the perturbative model developed in [16]. This model relies on expansion of the Hamiltonian up to second order in Φ_{zpf}/Φ_0 , which is still applicable to our strongly coupled system. The resonator shift is determined by the ABSs in the ground state, which is described by

$$\delta f_r = -2 \left(\frac{\pi \Phi_{zpf}}{\Phi_0} \right)^2 \frac{\partial^2 f_A}{\partial \varphi^2} + \left(\frac{g_c(\varphi)}{2\pi} \right)^2 \left(\frac{2}{f_A} - \frac{1}{f_A - f_r} - \frac{1}{f_A + f_r} \right), \quad (\text{C3})$$

with the phase-dependent coupling rate

$$\frac{g_c(\varphi)}{2\pi} = \frac{\Phi_{zpf}}{\Phi_0} \sqrt{(1 - \tau)} \left(-\frac{\partial f_A}{\partial \varphi} \right) \tan(\varphi/2), \quad (\text{C4})$$

where the pair transition frequency is expressed through its energy as $f_A(\varphi) = 2E_A(\varphi)/h$. Here, we introduced a single channel and neglected all the possible higher energy states, including the continuum of states above the superconducting gap, which is known to contribute to the inductive response of a finite-length weak link [26, 34]. We also neglected the inductive energy of the shared inductance, which is generally true only when the supercurrent in the weak link is sufficiently small. However, this simple model demonstrated good correspondence between the extracted value of the coupling, and the one directly observed in spectroscopy (e.g., in Fig. 3, see the main text), which justifies its validity.

In our fits, we used the least squares method. When single-tone spectra in Fig. 3(b) and Fig. 4(b) were fitted, the data set was multiplied by $f_A - f_r$ to eliminate the divergence in Eq. (C3).

Appendix D: Relation between the phase across the weak link and the applied flux

In our devices, the loop inductance comprises the highly inductive NbTiN film with a total inductance of $2l \approx 10$ nH. When external flux is applied, part of the phase drops across the loop inductance, causing the self-screening effect [35]:

$$\varphi = \frac{2\pi}{\Phi_0} (\Phi - 2lI_s), \quad (\text{D1})$$

where the supercurrent through the weak link is given by

$$I_s = \frac{-2e}{\hbar} \sum_p \frac{\partial E_A^p}{\partial \varphi}. \quad (\text{D2})$$

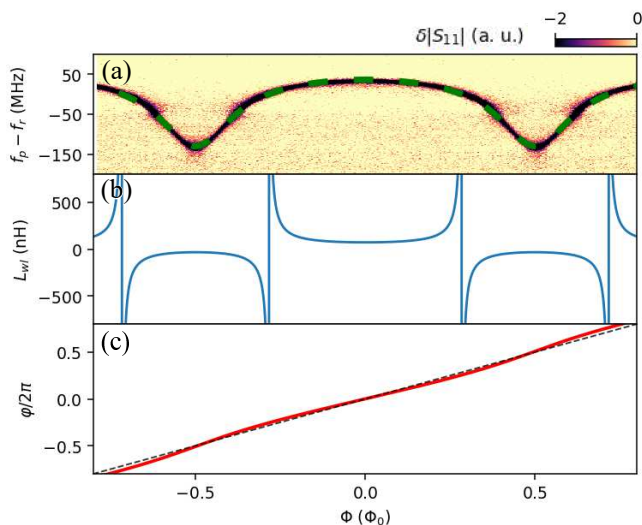


FIG. 7. (a) Single-tone spectrum measured in Device 3 at $V_g = 1.5034$ V offset to the bare resonator frequency $f_r = 7.4685$ GHz. The frequency shift fit as a function of applied flux is denoted by the green dashed line. (b) Corresponding weak link inductance, derived from (D3, D4). (c) The red line represents the phase across the weak link φ as a function of the applied flux Φ . For comparison, the black dashed line is plotted in the absence of self-screening ($2l = 0$).

Here the sum is taken by all ABSs with dispersions E_A^p . The full spectrum of ABSs residing in the weak link spans up to $2\Delta_{Al}$ and, therefore, is usually not accessible in experiments.

However, it is possible to estimate the self-screening effect in the dispersive regime. Considering the circuit shown in Fig. 1(b) classically, we obtain the resonator frequency shift that arises from shunting the $2l$ part of the resonator inductance with the phase-dependent weak link inductance $L_{wl}(\varphi)$:

$$\frac{\delta f}{f_r} = -\frac{\delta L}{2(2L_r)}, \quad (\text{D3})$$

where $2L_r$ is the total resonator inductance and

$$\delta L = 2L_r - 2l + \frac{2lL_{wl}}{2l + L_{wl}} - 2L_r = -\frac{(2l)^2}{2l + L_{wl}}. \quad (\text{D4})$$

Thus, the weak link inductance can be directly retrieved from the single-tone spectra in dispersive regime. The total supercurrent is related to the weak link inductance as [36]:

$$L_{wl}(\varphi)^{-1} = \frac{2\pi}{\Phi_0} \frac{\partial I_s}{\partial \varphi}. \quad (\text{D5})$$

We analyze the self-screening effect, using the single-tone spectroscopy data obtained for Device 3 at $V_g = 1.5034$ V, see Fig. 7(a). In this regime, no avoided crossing is observed, but the resonator shift is reasonably large (about 150 MHz), which implies that one or a

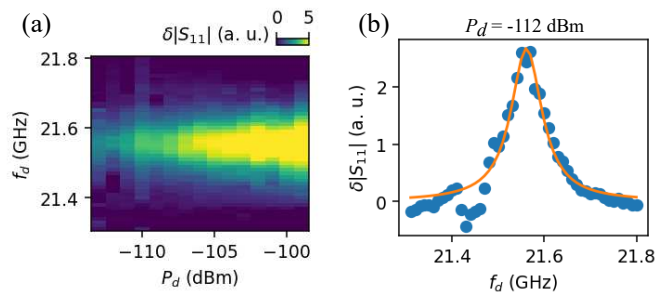


FIG. 8. (a) Power spectrum for the Device 3 at $V_g = 3.962$ V and $\varphi = 0$. (b) Linecut of (a) at low power $P_d = -112$ dBm with a Lorentzian fit.

few ABS with moderate transmission are present in the weak link, resulting in a relatively large supercurrent. The frequency shift fit is obtained by introducing one channel with $\Delta'/h = 17$ GHz, $\tau = 0.68$, $\Phi_{zpf} = 0.025\Phi_0$. Using (D3) and (D4), we extract L_{wl} as a function of the applied flux, see Fig. 7(b). Further, under the assumption of negligible self-screening $\varphi \approx 2\pi\Phi/\Phi_0$, we calculate the supercurrent by integrating (D5), and plug it into (D1) to estimate the self-screening. Fig. 7(c) shows that $\varphi \approx 2\pi\Phi/\Phi_0$ was indeed a reasonable approximation, and self-screening can be neglected.

Appendix E: Power spectrum

Fig. 8(a) represents the power spectrum, obtained for one of the PT observed in Device 2 at $\varphi = 0$. A low-power spectral line can be used to estimate the lower bound of the inhomogeneous dephasing time T_2^* in this device [37]. A linecut at $P_d = -112$ dBm is shown in Fig. 8(b). A Lorentzian fit to the spectral line fit reveals the full width at half maximum $f_{\text{FWHM}} \approx 82$ MHz. We estimate the lower bound of the inhomogeneous dephasing time as $T_2^* \gtrsim 1/\pi f_{\text{FWHM}} \approx 4$ ns, a smaller value, compared to the previously reported [11].

-
- [1] A. Blais, A. L. Grimsmo, S. M. Girvin, and A. Wallraff, Circuit quantum electrodynamics, *Rev. Mod. Phys.* **93**, 025005 (2021).
- [2] X. Mi, J. V. Cady, D. M. Zajac, P. W. Deelman, and J. R. Petta, Strong coupling of a single electron in silicon to a microwave photon, *Science* **355**, 156 (2016).
- [3] J. Clarke and F. K. Wilhelm, Superconducting quantum bits, *Nature* **453**, 1031 (2008).
- [4] A. Wallraff, D. I. Schuster, A. Blais, L. Frunzio, R.-S. Huang, J. Majer, S. Kumar, S. M. Girvin, and R. J. Schoelkopf, Strong coupling of a single photon to a superconducting qubit using circuit quantum electrodynamics, *Nature* **431**, 162 (2004).
- [5] P. Forn-Díaz, L. Lamata, E. Rico, J. Kono, and E. Solano, Ultrastrong coupling regimes of light-matter interaction, *Rev. Mod. Phys.* **91**, 025005 (2019).
- [6] T. Niemczyk, F. Deppe, H. Huebl, E. P. Menzel, F. Hocke, M. J. Schwarz, J. J. Garcia-Ripoll, D. Zueco, T. Hümmer, E. Solano, A. Marx, and R. Gross, Circuit quantum electrodynamics in the ultrastrong-coupling regime, *Nat. Phys.* **6**, 772 (2010).
- [7] Y. Wang, C. Guo, G.-Q. Zhang, G. Wang, and C. Wu, Ultrafast quantum computation in ultrastrongly coupled circuit QED systems, *Sci. Rep.* **7**, 1 (2017).
- [8] I. O. Kulik, Macroscopic Quantization and the Proximity Effect in S-N-S Junctions, *Soviet Journal of Experimental and Theoretical Physics* **30**, 944 (1969).
- [9] C. W. J. Beenakker and H. van Houten, Josephson current through a superconducting quantum point contact shorter than the coherence length, *Phys. Rev. Lett.* **66**, 3056 (1991).
- [10] A. Zazunov, V. S. Shumeiko, E. N. Bratus', J. Lantz, and G. Wendin, Andreev level qubit, *Phys. Rev. Lett.* **90**, 087003 (2003).
- [11] M. Hays, G. de Lange, K. Serniak, D. J. van Woerkerk, D. Bouman, P. Krogstrup, J. Nygård, A. Geresdi, and M. H. Devoret, Direct microwave measurement of andreev-bound-state dynamics in a semiconductor-nanowire Josephson junction, *Phys. Rev. Lett.* **121**, 047001 (2018).
- [12] P. Zellekens, R. S. Deacon, P. Perla, D. Grützmacher, M. I. Lepsa, T. Schäpers, and K. Ishibashi, Microwave spectroscopy of Andreev states in InAs nanowire-based hybrid junctions using a flip-chip layout, *Commun. Phys.* **5**, 1 (2022).
- [13] M. Hays, V. Fatemi, D. Bouman, J. Cerrillo, S. Diamond, K. Serniak, T. Connolly, P. Krogstrup, J. Nygård, A. L. Yeyati, A. Geresdi, and M. H. Devoret, Coherent manipulation of an Andreev spin qubit, *Science* **373**, 430 (2021).
- [14] L. Tosi, C. Metzger, M. F. Goffman, C. Urbina, H. Pothier, S. Park, A. L. Yeyati, J. Nygård, and P. Krogstrup, Spin-orbit splitting of andreev states revealed by microwave spectroscopy, *Phys. Rev. X* **9**, 011010 (2019).
- [15] M. Hays, V. Fatemi, K. Serniak, D. Bouman, S. Diamond, G. de Lange, P. Krogstrup, J. Nygård, A. Geresdi, and M. H. Devoret, Continuous monitoring of a trapped superconducting spin, *Nat. Phys.* **16**, 1103 (2020).
- [16] C. Metzger, S. Park, L. Tosi, C. Janvier, A. A. Reynoso, M. F. Goffman, C. Urbina, A. Levy Yeyati, and H. Pothier, Circuit-QED with phase-biased Josephson weak links, *Phys. Rev. Res.* **3**, 013036 (2021).
- [17] P. Krogstrup, N. L. B. Ziino, W. Chang, S. M. Albrecht, M. H. Madsen, E. Johnson, J. Nygård, C. M. Marcus, and T. S. Jespersen, Epitaxy of semiconductor-superconductor nanowires, *Nat. Mater.* **14**, 400 (2015).
- [18] C. Padurariu and Yu. V. Nazarov, Theoretical proposal for superconducting spin qubits, *Phys. Rev. B* **81**, 144519 (2010).
- [19] M. Pita-Vidal, J. J. Westdorp, and C. K. Andersen, Blueprint for All-to-All-Connected Superconducting Spin Qubits, *PRX Quantum* **6**, 010308 (2025).
- [20] H. Lu, I. A. Day, A. R. Akhmerov, B. van Heck, and V. Fatemi, Kramers-protected hardware-efficient error correction with Andreev spin qubits, *arXiv* 10.48550/arXiv.2412.16116 (2024), 2412.16116.
- [21] S. Abay, D. Persson, H. Nilsson, F. Wu, H. Q. Xu, M. Fogelström, V. Shumeiko, and P. Delsing, Charge transport in InAs nanowire Josephson junctions, *Phys. Rev. B* **89**, 214508 (2014).
- [22] M. H. Devoret, S. Girvin, and R. Schoelkopf, Circuit-QED: How strong can the coupling between a Josephson junction atom and a transmission line resonator be?, *Ann. Phys.* **519**, 767 (2007).
- [23] A. Stockklauser, P. Scarlino, J. V. Koski, S. Gasparinetti, C. K. Andersen, C. Reichl, W. Wegscheider, T. Ihn, K. Ensslin, and A. Wallraff, Strong Coupling Cavity QED with Gate-Defined Double Quantum Dots Enabled by a High Impedance Resonator, *Phys. Rev. X* **7**, 011030 (2017).
- [24] J. E. Sestoft, M. Marnauza, D. Olsteins, T. Kanne, R. D. Schlosser, I.-j. Chen, K. Grove-Rasmussen, and J. Nygård, Shadowed versus Etched Superconductor-Semiconductor Junctions in Al/InAs Nanowires, *Nano Lett.* **24**, 8394 (2024).
- [25] S. Park and A. L. Yeyati, Andreev spin qubits in multichannel Rashba nanowires, *Phys. Rev. B* **96**, 125416 (2017).
- [26] V. Fatemi, P. D. Kurilovich, M. Hays, D. Bouman, T. Connolly, S. Diamond, N. E. Frattini, V. D. Kurilovich, P. Krogstrup, J. Nygård, A. Geresdi, L. I. Glazman, and M. H. Devoret, Microwave Susceptibility Observation of Interacting Many-Body Andreev States, *Phys. Rev. Lett.* **129**, 227701 (2022).
- [27] M. Zgirski, L. Bretheau, Q. Le Masne, H. Pothier, D. Esteve, and C. Urbina, Evidence for Long-Lived Quasiparticles Trapped in Superconducting Point Contacts, *Phys. Rev. Lett.* **106**, 257003 (2011).
- [28] J. H. Ungerer, A. Pally, A. Kononov, S. Lehmann, J. Ridderbos, P. P. Potts, C. Thelander, K. A. Dick, V. F. Maisi, P. Scarlino, A. Baumgartner, and C. Schönenberger, Strong coupling between a microwave photon and a singlet-triplet qubit, *Nat. Commun.* **15**, 1 (2024).
- [29] C. METZGER, *Spin & charge effects in Andreev Bound States*, Ph.D. thesis, Service de physique de l'état condensé, France, Quantronics Group, France, Saclay (2022).
- [30] H. Lu, D. F. Bofill, Z. Sun, T. Kanne, J. Nygård, M. Kjaergaard, and V. Fatemi, Andreev spin relaxation time in a shadow-evaporated InAs weak link, *arXiv* 10.48550/arXiv.2501.11627 (2025), 2501.11627.

- [31] A. J. Annunziata, D. F. Santavicca, L. Frunzio, G. Catelani, M. J. Rooks, A. Frydman, and D. E. Prober, Tunable superconducting nanoinductors, *Nanotechnology* **21**, 445202 (2010).
- [32] J. Bardeen, L. N. Cooper, and J. R. Schrieffer, Theory of superconductivity, *Phys. Rev.* **108**, 1175 (1957).
- [33] S. Probst, F. B. Song, P. A. Bushev, A. V. Ustinov, and M. Weides, Efficient and robust analysis of complex scattering data under noise in microwave resonators, *Review of Scientific Instruments* **86**, 024706 (2015).
- [34] P. D. Kurilovich, V. D. Kurilovich, V. Fatemi, M. H. Devoret, and L. I. Glazman, Microwave response of an Andreev bound state, *Phys. Rev. B* **104**, 174517 (2021).
- [35] P. Jung, S. Butz, S. V. Shitov, and A. V. Ustinov, Low-loss tunable metamaterials using superconducting circuits with Josephson junctions, *Appl. Phys. Lett.* **102**, 062601 (2013).
- [36] A. Paila, D. Gunnarsson, J. Sarkar, M. A. Sillanpää, and P. J. Hakonen, Current-phase relation and Josephson inductance in a superconducting Cooper-pair transistor, *Phys. Rev. B* **80**, 144520 (2009).
- [37] K. D. Petersson, J. R. Petta, H. Lu, and A. C. Gosard, Quantum coherence in a one-electron semiconductor charge qubit, *Phys. Rev. Lett.* **105**, 246804 (2010).